Residual Structure in Islet Amyloid Polypeptide Mediates Its Interactions with Soluble Insulin†

Lei Wei, Ping Jiang, Yin Hoe Yau, Heike Summer, Susana Geifman Shochat, Yuguang Mu,* and Konstantin Pervushin*

School of Biological Sciences, Nanyang Technological University, 60 Nanyang Drive, Singapore 637551

Received November 13, 2008; Revised Manuscript Received January 15, 2009

ABSTRACT: Islet amyloid polypeptide (IAPP), a 37-amino acid polypeptide hormone of the calcitonin family, is colocalized and cosecreted with insulin in secretory granules of pancreatic islet β cells. IAPP can assemble into toxic oligomers and amyloid fibrils, a hallmark of type 2 diabetes. Its interactions with insulin in the secretory granules might influence the formation of cytotoxic oligomers and amyloid fibrils. Presented NMR analysis shows that IAPP, free in solution and in complex with insulin, retains elements of residual secondary structure. NMR chemical shifts and ^{15}N relaxation data as well as 49 ns replica exchange molecular dynamic simulations indicate that the transiently populated helical structure in residues 11−18 is essential for interactions with insulin. These interactions are mediated by salt bridges between positively charged residues Arg11 or Arg18 of rat IAPP and Glu13 of insulin B chain as well as by hydrophobic interactions flanking the salt bridges. The insulin binding region is composed of the same amino acids in amyloidogenic human IAPP and soluble rat IAPP (with the sole exception of His/Arg-18), implying the same binding mode for both hormones. This His/Arg-18 mutation results in reduced affinity binding of human IAPP to insulin in comparison to rat IAPP as it is detected by surface plasmon resonance biosensor analysis. Implications of the described interactions between soluble forms of IAPP and insulin in preventing oligomerization of human IAPP are discussed.

Islet amyloid polypeptide (IAPP[1] or amylin), a 37-amino acid polypeptide hormone of calcitonin family, is coexpressed and cosecreted with insulin by pancreatic β cells in the islets of Langerhans (*1*). Although the exact physiological function of IAPP remains under investigation, it is shown to control plasma glucose levels in concert with insulin (*2*). IAPP aggregation and formation of fibrillar amyloid deposits in the extracellular space of pancreatic β cells are closely associated with type 2 diabetes (T2D) (*3, 4*). The amyloid formation of IAPP is a result of its misfolding, leading to the formation of linear fibrils with cross-β structure (*5*). Increasing evidence suggests that amyloidogenic IAPP plays an important role in T2D pathogenesis. IAPP, in the species known to develop T2D such as human, monkey, and cat, is amyloidogenic. In contrast, IAPP is not amyloidogenic in rats and mice, which do not develop T2D (*6*). Furthermore, transgenic mice expressing human IAPP (hIAPP) develop T2D when high expression rates of hIAPP occur especially in an obesity background (*7*−*9*). The underlying mechanism of diabetes in hIAPP transgenic mice is deficit in β-cell mass because of increased β-cell apoptosis (*10, 11*). In vitro experiments demonstrated that IAPP fibril formation can cause death of β-cells by inducing apoptosis (*12*). More recent reports suggest that soluble IAPP oligomers formed in the prefibrillar stage, rather than mature amyloid fibrils, are the most cytotoxic species that induce β-cell apoptosis (*10, 13, 14*). Inhibition of IAPP fibril formation, but not formation of toxic IAPP oligomers, does not prevent β-cells from apoptosis induced by either overexpression or application of IAPP (*15*). Similarly, studies on amyloidogenic peptide Aβ in Alzheimer's disease (AD) demonstrated that soluble oligomers of Aβ, but not monomers or insoluble amyloid fibrils, lead to synaptic dysfunction in the brains of AD patients (*16*). Soluble amyloid oligomers derived from different types of amyloidogenic proteins such as Aβ, α-synuclein, IAPP, and prion peptide 106−126, despite having different amino acid sequences, share a common immunoreactivity, which implies they likely share a common mechanism of cytotoxicity (*13*). In addition, IAPP−membrane interactions are implicated in IAPP-dependent toxicity by both accelerating oligomer formation and disrupting membrane integrity and permeability (*17*).

Since the amyloidogenic IAPP is clearly involved in T2D pathogenesis, it is important to understand what factors affect its cytotoxicity and fibril formation in health. IAPP remains soluble in secretory vesicles at an estimated concentration of 0.8−4 mM in vivo (*18*), which far exceeds its solubility

* To whom correspondence should be addressed. Phone (office): +65-6316-7993 (K.P.), +65-6316-2885 (Y.M.). Fax: +65-6791-3856 (K.P.), +65-6791-3856 (Y.M.). E-mail: kpervushin@ntu.edu.sg (K.P.), ygmu@ntu.edu.sg (Y.M.).

† Y.M. gratefully acknowledges support from the academic research fund AcRF Tier 2 (T206B3210RS) by the MOE.

[1] Abbreviations: CD, circular dichroism; DSS, 2,2-dimethyl-2-silapentane-5-sulfonate, sodium salt; HFIP, 1,1,1,3,3,3-hexafluoro-2-propanol; hIAPP, human islet amyloid polypeptide; HPLC, high-performance liquid chromatography; IAPP, islet amyloid polypeptide; IPTG, isopropyl-β-D-thiogalactopyranoside; MALDI-MS, matrix-assisted laser desorption/ionization mass spectrometry; MD, molecular dynamic simulations; NMR, nuclear magnetic resonance; REMD, replica exchange molecular dynamics; rIAPP, rat islet amyloid polypeptide; SPR, surface plasmon resonance; T2D, type 2 diabetes.

10.1021/bi802097b CCC: $40.75
Published on Web 01/15/2009

in aqueous solution at the same pH (5−6) in vitro (*19*). Colocalized insulin, which has an effective concentration of about 40 mM, has been suggested to stabilize IAPP and inhibit its misfolding and amyloid formation in its secretory pathway (*19*−*21*), but the mechanism of this inhibition has not been yet determined. Specific interactions between IAPP and insulin were demonstrated by immunoprecipitation and surface plasmon resonance (SPR) experiments in vitro (*22*). Insulin has been shown to prevent the transition of IAPP from random coil to β-sheet and subsequent amyloid fibril formation, implying that it is an exceptionally potent inhibitor (*22*−*25*). Even in the presence of lipid membranes, lipid-catalyzed IAPP fibril formation can still be strongly inhibited by insulin at the concentrations found in the β-cell secretory granules (*25*). Structural characterization of the molecular determinants that mediate IAPP−insulin interactions is essential to understanding the mechanism preventing IAPP cytotoxicity in health and disease. However, low solubility and high fibrillogenesis propensity render it challenging to map the binding interface of the hIAPP−insulin complex. One approach to overcome this challenge is to use a stabilized analogue of IAPP from either other variants or mutagenesis. The rat variant of IAPP (rIAPP) does not misfold to form amyloid fibrils in an aqueous environment, although it differs in only six residues from hIAPP (*6*). Three prolines at positions 25, 28, and 29 are reported to be responsible for the inhibition of amyloid fibrils formation (*6*). rIAPP is shown to adopt similar structures to the prefibrillar states of hIAPP in a physiological buffer (*26*). Freshly dissolved rIAPP and hIAPP exhibit a similar ability to insert into negatively charged phospholipid membranes, and both of them form α-helical structures (*27, 28*). rIAPP can permeate synthetic vesicles under conditions that permit rIAPP membrane binding (*29*). Moreover, rIAPP is also shown to bind insulin specifically like hIAPP (*22*). Therefore, rIAPP could be used as a soluble analogue of hIAPP to study its interaction with insulin.

In this study, we aim to identify the structural basis of the interaction between soluble forms of IAPP and insulin by NMR and replica exchange molecular dynamics (REMD) simulations. Our result indicates that insulin binds to IAPP (residues 1−18) via salt bridges and hydrophobic interactions. The interaction interface is conveniently provided by the residual structures found in IAPP and the stable 3D fold of native insulin.

MATERIALS AND METHODS

Expression and Purification of ^{15}N Uniformly Labeled rIAPP and hIAPP. The peptides corresponding to the mature rIAPP and hIAPP were expressed and purified according to the protocol described by Williamson and Miranker (*30*) with the following modifications: IAPPs were cloned and expressed using pTXB 1 vector (New England Biolabs, Inc.). The insert sequences were designed and comprised of the coding sequences of the leader sequence [MKIEEG(NANP)$_3$E] (*30*), IAPP, and a part of the intein sequence in pTXB 1 flanked by NdeI and SpeI compatible overhangs. The coding sequences of IAPP were optimized for expression in *Escherichia coli*. Two oligonucleotides comprising the sense and antisense strands of the insert (purchased from Integrated DNA Technologies, Inc.) were annealed to obtain the double-stranded insert sequence in buffer containing 20 mM Tris, 2 mM $MgCl_2$, and 50 mM NaCl. The insert sequence was ligated into the pTXB 1 vector which had been treated with NdeI and SpeI using T4 DNA ligase (New England Biolabs, Inc.). The constructed plasmid was cloned in DH5α *E. coli* cells and verified by sequencing. To express ^{15}N uniformly labeled IAPP, the construct was transformed into *E. coli* BL21 cells, grown to an absorbance (600 nm) of 1.0 in M9 minimal medium with 100 μg/mL ampicillin at 37 °C and induced with 1 mM IPTG for 4 h expression. Cells were collected, and the protein was purified according to the above-mentioned protocol (*30*). In brief, cells were resuspended in 20 mL of column buffer (20 mM HEPES, 0.1 mM EDTA, 50 mM NaCl, and 2 M urea, pH 8) and lysed by a sonicator or homogenizer. The cleared soluble cell lysate was applied into the chitin (New England Biolabs, Inc.) column pre-equilibrated with column buffer. The column was washed quickly with 10 column volumes of column buffer followed by 3 column volumes of cleavage buffer (column buffer plus 100 mM DTT and 2 M ammonium bicarbonate, pH 8). After the overnight on-column cleavage, the bound peptide was eluted by using 1 column volume of the elution buffer (column buffer plus 2 M ammonium bicarbonate, pH 8). The fusion peptides containing IAPP were dialyzed at 4 °C using the Spectra/Por 6 1000 MWCO tubing membrane. Both peptides were digested by V8 protease (Roche) and purified by reverse-phase HPLC on a C18 column using 0−60% acetronitrile (ACN)/water gradient with 0.045% trifluoroacetic acid (TFA) over 60 min. The yield of ^{15}N labeled IAPP is about 2 mg per liter of minimal medium. Thus, produced IAPPs were verified by using matrix-assisted laser desorption/ionization mass spectrometry (MALDI-MS).

NMR Spectroscopy. All NMR experiments were performed using the Bruker Advance II 700 MHz spectrometer at 25 °C. Natural abundance HNCA, ^{15}N-TOCSY-HSQC (TOCSY = total correlation spectroscopy, HSQC = heteronuclear single quantum coherence; τ_{mix} = 120 ms) and ^{15}N-NOESY-HSQC (NOESY = nuclear Overhauser enhancement spectroscopy; τ_{mix} = 200 ms), [^{1}H, ^{15}N] heteronuclear nuclear Overhauser effect (NOE), ^{15}N relaxation (R_1 and R_2), and ^{15}N relaxation dispersion experiments (*31*) were collected using ^{15}N uniformly labeled rIAPP. 2D [^{1}H, ^{15}N] HSQC spectra were acquired to map the insulin binding region of rIAPP. The data were first collected on a sample containing 50 μM ^{15}N uniformly labeled rIAPP (in 5 mM potassium phosphate buffer, 10 mM KCl, 3% D_2O, pH 6). The sample was subsequently titrated with 0.5 mM, 1.0 mM, and 1.5 mM unlabeled insulin, and [^{1}H, ^{15}N] HSQC spectra were collected. Two-dimensional TOCSY and NOESY (τ_{mix} = 150 ms) were carried out on 0.5 mM insulin (in 5 mM sodium phosphate buffer, 10 mM NaCl, 3% D_2O, pH 6) for assignment of ^{1}H resonances. ^{15}N-filtered NOESY (τ_{mix} = 150 ms),^{15}N-TOCSY-HSQC (τ_{mix} = 120 ms), ^{15}N-NOESY-HSQC (τ_{mix} = 200 ms), [^{1}H, ^{15}N] heteronuclear NOE, and relaxation (R_1 and R_2) spectra were measured using a mixed sample containing 0.5 mM insulin and 0.5 mM ^{15}N uniformly labeled rIAPP (in 5 mM sodium phosphate buffer, 10 mM NaCl, 3% D_2O, pH 6). ^{15}N relaxation dispersion was also measured by using the published pulse sequence (*31*). The spectra were analyzed with CARA (www.nmr.ch). The manually generated peak list and the chemical shift assign-

ment were used as the input for structure calculations by CYANA 2.0 (*32*). The chemical shifts were referenced to 2,2-dimethyl-2-silapentane-5-sulfonate (DSS) directly for ^{1}H and indirectly for ^{13}C and ^{15}N spins.

Molecular Dynamics (MD) Simulations. Forty-nine nanoseconds long REMD simulations (*33, 34*) of the full length insulin (PDB; 1G7A) complexed with rodent or human IAPP fragments comprising residues 9−20 ($rIAPP_{9-20}$) were performed. The N- and C-termini of $IAPP_{9-20}$ were capped by ACE and NME, respectively. Initial extended and folded configurations of IAPP and insulin, respectively, placed 15 Å apart, were used. A dodecahedron box, the size of 50 Å, containing 2498 and 2519 water molecules (SPC model) for rat and human IAPP was used. Each REMD run contained 24 replicas to cover the temperature range from 315.0 to 394.4 K with the exchange rates maintained at around 30% using the Gromacs simulation package (*35*) with OPLSAA all-atomic force field (*36*). During the simulation, the positions of backbone atoms of insulin were restrained. All covalent bonds involving hydrogen atoms were constrained according to LINCS protocol (*37*). The protein and the water species were separately coupled to the external heat bath with the relaxation time of 0.1 ps. The replica exchange was attempted at every 1000th integration step (2 ps). The structure snapshots were outputted every 1 ps resulting in the ensemble of 49 000 structures. The electrostatic interactions were treated using the particle mesh Ewald method (*38*) with the cutoff set to 9 Å. For the van der Waals interactions, the corresponding cutoff was set to 14 Å.

Binding Analysis of Insulin and IAPP Using SPR. SPR biosensor experiments were conducted at 25 °C using a Biacore 3000 instrument docked with the research-grade SA chips (Biacore AB, Uppsala, Sweden). Both biotinylated hIAPP and rIAPP (USBiological) were first dissolved in 100% 1,1,1,3,3,3-hexafluoro-2-propanol (HFIP) at 1 mM, diluted into 10 mM sodium acetate, pH 5.0 (dilution level 1:5000), and injected at 10 μL/min over flow cells 2 and 3, respectively. The levels of hIAPP and rIAPP captured by streptavidine (SA) on the surface were 200 and 700 RU, respectively. The flow cell 1 was maintained as the reference (SA unmodified surface). The surface was stabilized with continuous flow of HBS-EP (10 mM HEPES, 150 mM NaCl, 3.4 mM EDTA, 0.0005% surfactant P20, pH 7.4) at a rate of 10 μL/min for 10−15 min. Insulin (Sigma) was diluted in a two-fold manner with HBS-EP buffer and injected sequentially over the flow cells 1−3 for 2 min at 10 μL/min. The sensorgrams were double-referenced (responses were corrected with both blank buffer injections and the response from the reference flow cell) (*39*). The responses were fit using the steady-state binding model. The experiments were repeated 5 times.

RESULTS

Residual Structure of rIAPP. The [^{1}H, ^{15}N] HSQC spectrum of rIAPP is well resolved, featuring narrow line widths and low dispersed amide proton chemical shifts (Supporting Information, Figure S1) compatible with the globally disordered structure of rIAPP in solution. The [^{1}H, ^{15}N] HSQC spectrum of hIAPP measured at significantly lower concentrations to reduce aggregation exhibits similar dispersion of chemical shifts as seen in rIAPP. The exhaustive assignment of resonances in this sample was hampered by aggregation, and the 3D structure was not calculated. For rIAPP, 20 conformers representing the solution structure of rIAPP were obtained using 281 interproton NOE constraints (Table 1). No overall compact structure can be detected as a result of the lack of long-range NOEs. The local structure revealed relatively well-defined regions at the N-terminus comprising residues 1−8 and 12−18 with the less than 0.5 Å average local root mean square deviation (rmsd) of backbone atoms (Figure 1a) with higher than average densities of medium-range NOEs (Figure 1b). Strong $d_{\alpha N}(i, i + 2)$ NOEs reveal the formation of a tight turn structure comprising residues 1−8 (Figures 1c and 2a) primarily imposed by the disulfide bond between Cys2 and Cys7. This tight turn structure is confirmed by H^{α} and C^{α} secondary shifts observed in this region (Figure 3). The region comprising residues 9−17 exhibits a pattern of $d_{\alpha N}(i, i + 3)$ and $d_{\alpha N}(i, i + 4)$ NOEs indicative of the presence of an α-helix (Figure 1c). However, the reduced amplitudes of H^{α} and C^{α} secondary shifts in this region point to an only transiently populated structure (Figure 3). Comparing observed $^{1}H^{\alpha}$ and $^{13}C^{\alpha}$ secondary shifts with the typical secondary shifts found in fully fledged helices (*40, 41*), the residues 9−17 of rIAPP are estimated to be 10−20% helical. Although [^{1}H, ^{15}N] heteronuclear NOEs observed for rIAPP were generally low, the continuous stretches of positive NOEs indicate higher backbone rigidity in the N-terminal region (Supporting Information, Figure S2a). Figure 2 shows the local structure detected at the N-terminus. The residues at the C-terminus constitute the least structured region as a

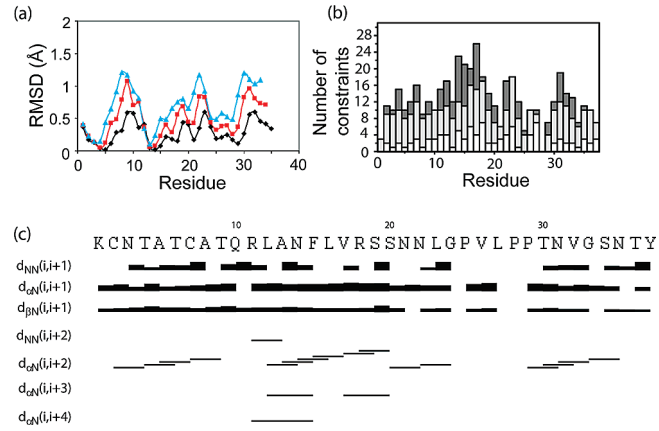

FIGURE 1: (a) Plot of the average local backbone rmsd's of three residues (black diamond), four residues (red squares), and five residues (cyan triangles) calculation window against the starting residue for the best 20 conformers. (b) Bar graph representing the number of intraresidual (white), short-range (light gray), and medium range (dark gray) $^{1}H-^{1}H$ distance constraints per residue used for structural calculations. (c) Summary of sequential and short- to medium-range $^{1}H-^{1}H$ NOE connectivities observed for H^{α}, H^{β}, and H^{N} in a 3D ^{15}N-NOESY-HSQC (τ_{mix} = 200 ms) spectrum of rIAPP. Bar thickness represents the intensity of $^{1}H-^{1}H$ NOE connectivity.

Table 1: Structural Restraints for the Best 20 Conformers Calculated by CYANA

total interproton restraints	281
short-range, $\|i - j\| \leq 1$	223
medium-range, $1 < \|i - j\| < 5$	58
long-range, $\|i - j\| \geq 5$	0
average assignments/constraint	1.00

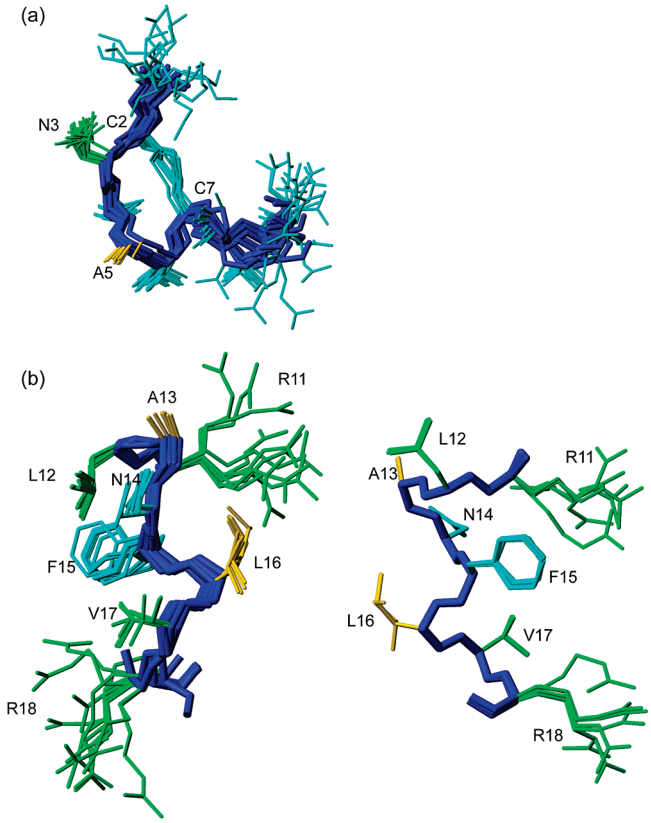

FIGURE 2: Residual structure of rIAPP at the N-terminus. (a) Structural ensemble of residues 1−10 which contains 18 structures. One disulfide bond is formed between two cysteine residues, C2 and C7. (b) Two structural ensembles of residues 11−18, which contain 11 structures (left) and 8 structures (right), respectively. The structures shown here are the best fit superimpositions of the backbones of all 20 structures (blue). The side chains are shown for residues with chemical shift perturbations (see Figure 4) $\Delta\delta \geq 0.008$ ppm (green), 0.006 ppm $\leq \Delta\delta < 0.008$ ppm (gold), and the rest (cyan) upon insulin binding.

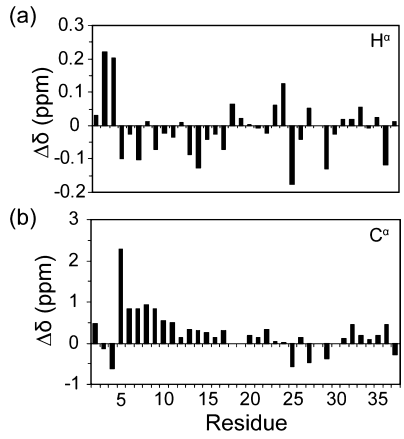

FIGURE 3: H^{α} secondary shift (a) and C^{α} secondary shift (b) for rIAPP. Secondary shift ($\Delta\delta$) was calculated by comparing our observed chemical shifts with random coil chemical shifts on a residue-by-residue basis (*58*).

result of lower [^{1}H, ^{15}N] heteronuclear NOEs as well as the ^{15}N R_1 relaxation rates (Supporting Information, Figure S2).

Mapping of Insulin−rIAPP Binding Interface. Chemical shift perturbations upon insulin binding were monitored in series of 2D [^{1}H, ^{15}N] HSQC for ^{15}N labeled rIAPP. Consistent changes of ^{1}H and ^{15}N chemical shifts were observed for several residues as function of insulin concentration not reaching saturation in the accessible concentration range, indicating weak but specific interactions (Figure 4a,b). The residues interacting with insulin are mainly located at the N-terminus of rIAPP at positions 1−18, with the largest perturbations seen for Arg11, Arg18, and their surrounding residues, Leu12, Ala13, Leu16, and Val17 (Figure 4a,b). In addition, in the presence of insulin, the cross peaks stemming from the backbone N−H of Cys2 and the side chain Nε−Hε moiety of Arg11 or Arg18 were detected in the HSQC spectra and otherwise broadened beyond detection (Supporting Information, Figure S1). We attributed this to the formation of a salt bridge between Arg11 and Arg18 side chains and acid groups of insulin. The exhaustive analysis of ^{15}N resolved NOESY of rIAPP in the presence of insulin did not show any new NOEs, indicating that the binding of insulin was not accompanied by significant structure consolidation. This is in line with ^{15}N relaxation dispersion data, showing that the exchange between free and bound to insulin rIAPP is faster than 1000 s^{-1}, the highest employed Carr-Purcell-Meiboom-Gill (CPMG) pulse sequence rate. Taken together, the data show that weak interactions between rIAPP and insulin might be primarily mediated by positively charged residues presented in the transiently populated local structure in residues 2−17 of rIAPP.

To identify the rIAPP binding region of insulin, ^{15}N filtered NOESY was measured for insulin upon ^{15}N rIAPP addition to eliminate the signals stemming from ^{15}N labeled rIAPP (Figure 5a,b). The detected IAPP binding region is mainly localized to the B chain of insulin. A segment of the B chain from Glu13 to Leu17 as well as residues His10 and Gly20 show apparent chemical shift perturbations delineating the binding interface (Figure 5b,c). In addition, residues Ser12, Leu13, Leu16, Tyr19, and Asn21 in the A chain show minor chemical shift perturbations and presumably are also involved in binding. Finally, the side chain Nε−Hε moiety of Arg22 (B chain) changes its position (Figure 5c), indicating likely participation of the side chain of Arg22 in the binding interface.

REMD Reconstruction of the rIAPP$_{9-20}$−Insulin Complex. Because of the absence of detectable intermolecular NOEs, we decided to reconstruct a 3D model of the rIAPP−insulin interaction interface using unrestrained REMD simulations. The resulting structures are evaluated through chemical shift perturbation data. A residue-based contact map between insulin and rIAPP$_{9-20}$ is constructed, showing three regions with high contact probabilities: (i) Glu13 (B chain) and Arg11 (rIAPP), (ii) Asn21 (A chain) and Arg11 (rIAPP), and (iii) Glu13 (B chain), His10 (B chain), and Arg18 (rIAPP; Figure 6). Simulations indicate preferential binding of rIAPP$_{9-20}$ to the B chain of insulin. The calculated contact map is generally consistent with NMR chemical shift perturbation data. NMR chemical shift information is utilized to filter the obtained structural snapshots. The selection criteria are based on the spatial proximity (closer than 4 Å) between heavy atoms of residues 14 and 17 (B chain), showing the highest chemical shift perturbations and residues 11, 12, 17, and 18 of rIAPP. The resulting structures are grouped into clusters (*42*). The center of the cluster with the largest occurrence is taken as the representative model (Figure 7).

In the model, rIAPP$_{9-20}$ takes a conformation with two short α-helical segments corresponding to the same α-helical

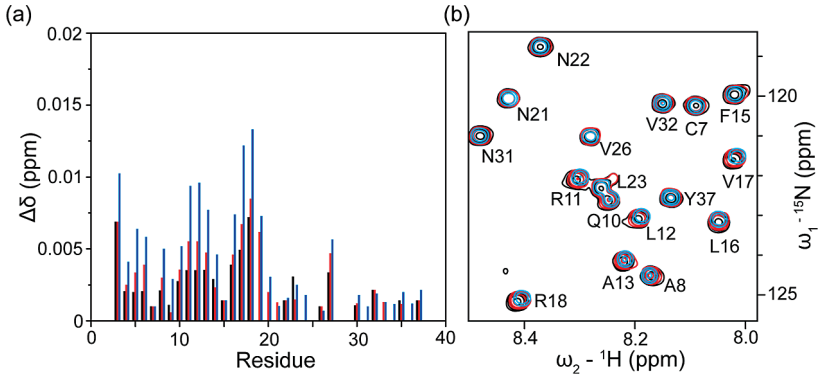

FIGURE 4: (a) Chemical shift perturbations ($\Delta\delta$ in ppm) of rIAPP in the presence of 0.5 mM, 1.0 mM, and 1.5 mM nonlabeled insulin (in black, red, and blue, respectively). The perturbations were calculated ($\Delta\delta = [(0.1\Delta\delta^N)^2 + (\Delta\delta^H)^2]^{1/2}$) for well-resolved peaks in the 2D [^{1}H, ^{15}N] HSQC spectra. The proline residues at positions 25, 28, and 29 were not included since prolines were not able to be detected by 2D [^{1}H, ^{15}N] HSQC. (b) Overlaid 2D [^{1}H, ^{15}N] HSQC spectra of uniformly labeled ^{15}N rIAPP alone (in black) and upon binding to 0.5 mM (in red) and 1.5 mM (in blue) insulin.

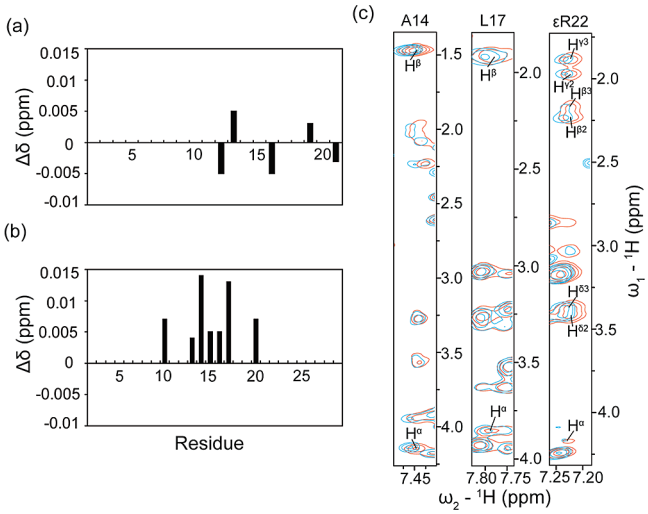

FIGURE 5: (a) Chemical shift perturbations ($\Delta\delta H^N$ in ppm) of the insulin A chain. (b) Chemical shift perturbations ($\Delta\delta H^N$ in ppm) of the insulin B chain upon IAPP addition. That $\Delta\delta H^N \leq 0.0025$ ppm is neglectable. (c) Fingerprint H^N region of B chain Ala14, Leu17, and H^ε region of B chain Arg22 in overlaid [^{1}H, ^{1}H] NOESY and ^{15}N filtered NOESY spectra of insulin. The proline residue at position 28 in the B chain was not included, since proline does not have an amide proton.

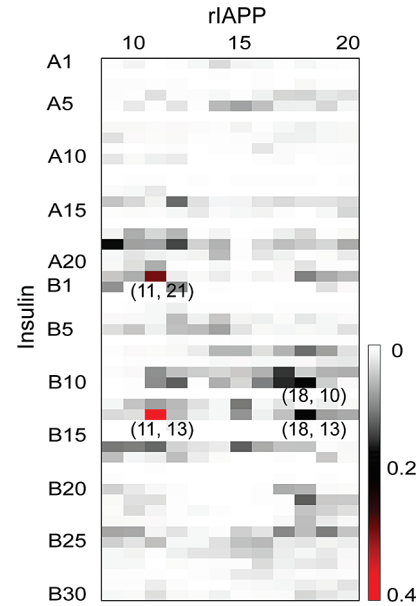

FIGURE 6: Residue contact probability map. One contact of two residues is counted when the distance between any two heavy atoms belonging to the two residues is less than 4 Å. The contact map is constructed on the basis of the last 45 ns of structural ensemble at a temperature of 315.0 K, which is normalized by the total structure snapshot number of 45 000. The coloring code label bar is shown on the right.

stretches found in NMR analysis. Arg11 of rIAPP is involved in a salt bridge with Glu13 (B chain) of insulin. The side chain of Leu12 of rIAPP is found to situate in a pocket formed by four hydrophobic residues, Phe1, Leu6, Ala14, and Leu17, and two polar residues, Gln4 and His10 on the B chain of insulin. Val17 and Arg18 of rIAPP located in the helical segment are found to be in a close proximity to the helical region of the B chain as well.

The REMD simulations of the human $IAPP_{9-20}$ and insulin complex are performed with a similar setup and protocols as described above with the exception that chemical shift perturbations measured with rIAPP were used for clustering. The contact maps obtained for $hIAPP_{9-20}$/insulin exhibit patterns similar to those of $rIAPP_{9-20}$ (data not shown). However, some significant differences can be still observed; in its neutral state, the contact probability of His18 with the insulin B chain residue Glu13 is 6%. The corresponding contact probability of Arg18 in rIAPP is 19%. The contact probability of Arg11 (hIAPP) with insulin B chain is 52%, which is larger than that of rIAPP (38%). These simulations indicate that the protonation state of His18 is likely to be important for insulin binding.

SPR Analysis of rIAPP and hIAPP Binding to Insulin. SPR was used to characterize IAPP−insulin interactions. Binding responses of soluble insulin onto both IAPPs are concentration dependent and specific (Figure 8a; there was practically no binding to the SA control surface). The affinity constants (K_D) were determined from a fit to a simple binding isotherm in an equilibrium analysis, and the values were found to be in the millimolar range for the interaction between both the IAPPs and the insulin (Figure 8a). Since we could not reach saturation of the surface because of the lack of solubility of insulin at sufficiently high concentrations and thus the calculated value of R_{max} could not be sufficiently precise, we have chosen, as a confirmation, to show the range for the values of the affinity constants by simulating the R_{eq}

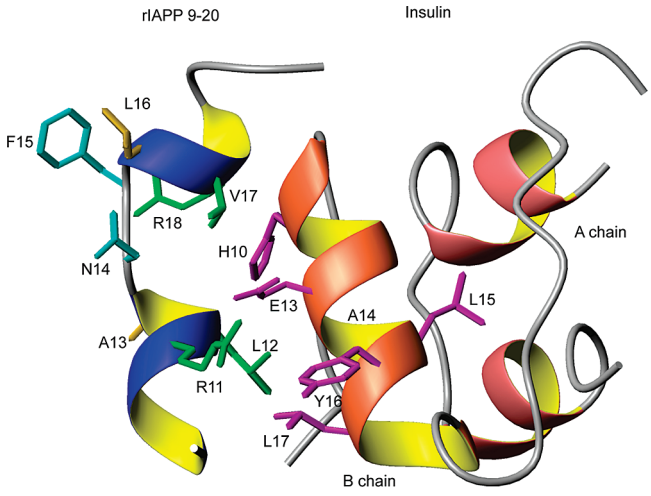

FIGURE 7: Structural representation of the IAPP−insulin complex. Ribbon drawings illustrate the backbone of $IAPP_{9-20}$ (blue) and the insulin A chain (light coral) and B chain (coral). Side chains of the residues involved in the interaction are illustrated according to their chemical shift perturbations for IAPP [see Figures 2b and 4] and insulin (magenta).

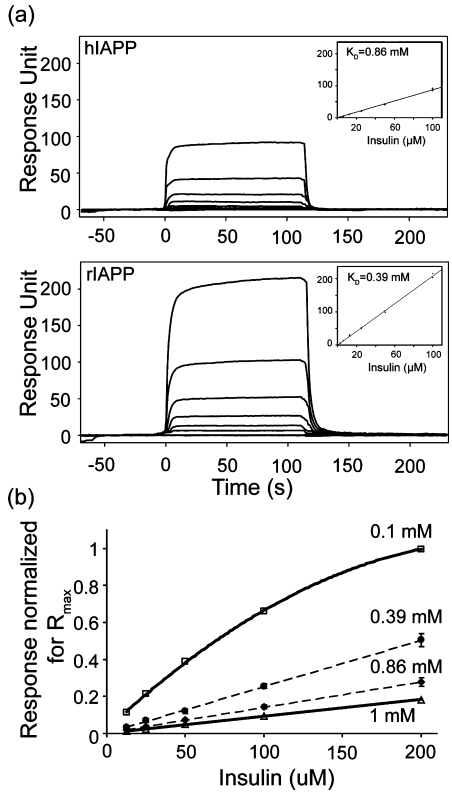

FIGURE 8: (a) Interaction analysis of insulin over immobilized hIAPP and rIAPP. Biotinylated hIAPP (above) and rIAPP (below) were immobilized onto an SA chip at the levels of 200 and 700 RU, respectively. Insulin (3.125, 6.25, 12.5, 25, 50, and 100 μM) was injected sequentially over the surfaces at 10 μL/min. The sensorgrams were fit using the steady state affinity model in Biaevaluation 4.1 software. (b) Experimental values of R_{eq} for the corrected sensorgrams compared to the simulated values for 0.1 mM and 1 mM for this interaction. The values for the affinity constants are between 0.1 mM and 1 mM.

values of the response versus insulin concentration for affinities of 0.1 mM and 1 mM and plotting the experimental R_{eq} values at the different concentrations of insulin. Figure 8b shows that the values for both interactions do fall between 0.1 mM and 1 mM.

DISCUSSION

Although previous biochemical studies have shown the inhibitory effects of insulin on IAPP cytotoxic species formation (*19*−*21*), little is known about the IAPP−insulin binding characteristics, interaction interface, and complex structure. Here, we provide a deeper view into the residual structure of IAPP and its interactions with insulin. Two local structural segments are observed at the N-terminus in our calculated structure ensemble by using $^1H-^1H$ NOE restraints: (i) a tight turn formed at residues 1−8 constrained by the disulfide bond between Cys2 and Cys7 and (ii) short helical regions at positions 11−18 (Figures 1 and 2). The helical region is also independently observed in MD simulations. In the complex with insulin, $rIAPP_{9-20}$ adopts a conformation comprising two short helical segments mediating insulin binding (Figure 7). The data suggest that the helical conformation of rIAPP is transiently populated and is in equilibrium with a random coil state. NMR chemical shift perturbations point to the N-terminal segment (residues 1−18), especially two positively charged residues Arg11 and Arg18 and their proximal hydrophobic residues Leu12, Ala13, Leu16, and Val17, to be involved in binding of insulin (Figure 4). Chemical shift mapping shows that the residues Glu13 to Leu17 in the insulin B chain interact with rIAPP (Figure 5). We suggest that the salt bridge between Arg11 or Arg18 of rIAPP and Glu13 of the insulin B chain is the main molecular determinant of the IAPP−insulin interactions. Previous studies employing peptide-array scanning identified residues 9−20 of the insulin B chain to be involved in binding with the region 7−19 of IAPP. It was proposed that insulin binds to the amyloid-formation recognition site of IAPP through a specific recognition mechanism mediated by aromatic interactions via π stacking (*23*). More specifically, the Tyr16 in the sequence of ALYLV at positions 14−18 of insulin B chain interacts with the Phe15 in the amyloid formation sequence ANFLV at positions 13−17 of IAPP and blocks the ability of IAPP to assemble into amyloid fibrils (*23*). This assumption was based on the hypothesis that π stacking interactions play a key role in the process of amyloid formation (*23*). In fact, the aromatic residues do play a role in fibril formation, but their role might be overemphasized in the above-mentioned hypothesis. Studies on a triple mutant of aromatic residues (F15L/F23L/Y37L) show that aromatic interactions influence the rate of fibril formation and fibril morphology, but they are not required for amyloid fibril formation of IAPP (*43*). Our data indicate no perturbation of the chemical shift of Phe15 upon insulin titration (Figure 4), ruling out the aromatic interactions (π stacking) as the primary determinant of the IAPP−insulin interactions. In contrast, we suggest the salt bridges formed between the charged residues of IAPP Arg11 or Arg18 (His18 in human variant) and insulin Glu13 (B chain) (Figures 6 and 7) as the main stabilizing interaction with hydrophobic interactions between the proximal hydrophobic residues of IAPP and insulin also contributing to binding affinity. The hydrophobic residue Leu12 or alternatively Val17 interacts with a hydrophobic patch on the surface of the B chain of insulin flanking the salt bridge (Figure 7).

We demonstrate that the amyloidogenic domain (residues 8−20) is located in this insulin-binding region of IAPP (residues 1−18). The region, residues 8−20 of both hIAPP and rIAPP, has been identified as an amyloidogenic domain capable of forming fibrils in a β-conformation (*44*). Previous study identified the sequence RLANFLVHSS (residues 11−20) as a major domain of molecular recognition for the IAPP self-assembly (*45*). The fragment LANFLV (residues 12−17) is able to accelerate IAPP self-assembly and IAPP induced cytotoxicity (*46*). Moreover, the N-terminal region of IAPP was shown to influence the overall kinetics of fibril formation (*47*). Considering the previous reports and the results in this work, we suggest that the IAPP self-assembly is driven by the hydrophobic domain LANFLV (residues 12−17) instead of the specific aromatic residue Phe15. The binding of insulin via the salt bridge and hydrophobic interactions sequesters the hydrophobic domain of IAPP and therefore may inhibit IAPP self-assembly into toxic oligomers and amyloid fibrils.

The peptide sequence within the region 20−29 of the IAPP is strongly associated with its amyloidogenicity of IAPP, and therefore, variances of the sequence within the 20−29 region have been used to explain the different cytotoxicity between hIAPP and rIAPP (*48*). The amyloidogenic fragment hIAPP 20−29 is shown to form a distorted type I β-turn in SDS micelles and disrupt phospholipid membranes upon its aggregation (*49, 50*). However, it has a much lower affinity to phospholipid membranes than the full-length peptide (*51*). In contrast, the N-terminal 1−19 region of hIAPP was found to disrupt membranes to a near identical extent as the full-length peptide (*51*). In addition, the nonamyloidogenic rIAPP also shows membrane disrupting activity, albeit significantly less effective than that of the hIAPP (*29, 51*). The greatly reduced toxicity can be ascribed to the single R18H mutation in the N-terminal 1−19 region of rIAPP (*51*). CD and recent NMR studies suggest that the N-terminal segment of the hIAPP peptide (residues 1−19) adopts a transmembrane orientation in mostly α-helical structure, while the C-terminal region is believed to locate outside the membrane in a disordered state (*17, 29, 51*−*53*). Moreover, infrared reflection absorption spectroscopy revealed that both hIAPP and rIAPP binds to phospholipid membranes by insertion of the N-terminal part of the peptide in an α-helical conformation (*28*). The interaction of hIAPP with the lipid interface is largely driven by electrostatic interactions, as the protein is able to strongly associate with negatively charged lipids exclusively (*28*). Our study shows that insulin also binds to the N-terminal region of IAPP mainly by electrostatic interactions (Figure 4). These results suggest the dual role of positively charged residues at the N-terminus in IAPP cytotoxicity and stability: they facilitate cytotoxicity and fibril formation when interacting with membranes but prevent IAPP misfolding when interacting with insulin. Therefore, insulin binding to the same N-terminal region of IAPP may reduce IAPP−membrane interactions by sequestering the charged residues leading to inhibition of the IAPP induced cytotoxicity. This mechanism could be used to explain the fact that lipid-catalyzed IAPP fiber formation is still strongly inhibited by insulin at the 100-fold excess concentration found in the β-cell secretory granule (*25*).

IAPP is wildly regarded as a natively unstructured protein as it adopts a random coil-like conformation in aqueous buffer. In this study, we find residual structure at the N-terminal fragment of IAPP mediating its interactions with insulin. It is still a puzzle what a role the dynamically flexible helical domain at the N-terminus might play in IAPP folding and misfolding. The N-terminal peptide of IAPP is in an α-helical conformation when bound to the membrane, which has been suggested to accelerate conversion to β-sheet rich fibrils in a cooperative manner (*28, 29, 53*). Both IAPP and Aβ in AD adopt α-helical conformation rather than β-sheet in their monomeric and oligomeric states (*29, 30, 54, 55*), and the oligomeric α-helix-containing intermediate was temporally correlated with fibrillogenesis of Aβ (*55*). Only the oligomeric but not monomeric IAPP is able to disrupt the membrane and induce cytotoxicity (*29*), supporting the finding that IAPP forms oligomers with a tertiary structure common to other amyloidogenic peptides despite having distinct monomeric structures (*13*). The monomeric IAPP with a conserved helical region was suggested to be its biological active state, which could bind to its receptor and trigger its hormonal activity such as glucose regulation (*30*). Constraining the bioactive conformation of the flexible IAPP might be a good strategy to generate stable high-affinity agonists of its biological function. The soluble IAPP analogue "Symlin" on the market is a hybrid of the human and rodent sequences (*56*). It has been used in combination therapy with insulin for diabetic patients, which could decrease degradation of the IAPP analogue−insulin complex and therefore increase their lifetime (*57*).

Multiple physiological interactions between IAPP and insulin were suggested as both binding of IAPP to crystalline insulin and the inhibition of IAPP fiber formation by soluble insulin are observed in vitro (*24, 25*). In this study, we have characterized the interaction of soluble forms of IAPP and insulin and the molecular determinants that mediate these interactions. This could not only outline the inhibition mechanisms of IAPP induced cytotoxicity by insulin but also provide the structural basis for the rational design of novel stabilizers preventing misfolding of IAPP and formation of cytotoxic species.

SUPPORTING INFORMATION AVAILABLE

Overlaid [^{1}H, ^{15}N] HSQC spectra and ^{15}N relaxation data of uniformly labeled ^{15}N rIAPP are shown. This material is available free of charge via the Internet at http://pubs.acs.org.

REFERENCES

1. Kahn, S. E., D'Alessio, D. A., Schwartz, M. W., Fujimoto, W. Y., Ensinck, J. W., Taborsky, G. J., Jr., and Porte, D., Jr. (1990) Evidence of cosecretion of islet amyloid polypeptide and insulin by beta-cells. *Diabetes 39*, 634–638.
2. Cooper, G. J. (1994) Amylin compared with calcitonin gene-related peptide: structure, biology, and relevance to metabolic disease. *Endocr. Rev. 15*, 163–201.
3. Cooper, G. J., Willis, A. C., Clark, A., Turner, R. C., Sim, R. B., and Reid, K. B. (1987) Purification and characterization of a peptide from amyloid-rich pancreases of type 2 diabetic patients. *Proc. Natl. Acad. Sci. U.S.A. 84*, 8628–8632.
4. Westermark, P., Wernstedt, C., O'Brien, T. D., Hayden, D. W., and Johnson, K. H. (1987) Islet amyloid in type 2 human diabetes mellitus and adult diabetic cats contains a novel putative polypeptide hormone. *Am. J. Pathol. 127*, 414–417.
5. Kajava, A. V., Aebi, U., and Steven, A. C. (2005) The parallel superpleated beta-structure as a model for amyloid fibrils of human amylin. *J. Mol. Biol. 348*, 247–252.

6. Westermark, P., Engstrom, U., Johnson, K. H., Westermark, G. T., and Betsholtz, C. (1990) Islet amyloid polypeptide: pinpointing amino acid residues linked to amyloid fibril formation. *Proc. Natl. Acad. Sci. U.S.A. 87*, 5036–5040.
7. Janson, J., Soeller, W. C., Roche, P. C., Nelson, R. T., Torchia, A. J., Kreutter, D. K., and Butler, P. C. (1996) Spontaneous diabetes mellitus in transgenic mice expressing human islet amyloid polypeptide. *Proc. Natl. Acad. Sci. U.S.A. 93*, 7283–7288.
8. Soeller, W. C., Janson, J., Hart, S. E., Parker, J. C., Carty, M. D., Stevenson, R. W., Kreutter, D. K., and Butler, P. C. (1998) Islet amyloid-associated diabetes in obese A(vy)/a mice expressing human islet amyloid polypeptide. *Diabetes 47*, 743–750.
9. Hoppener, J. W., Oosterwijk, C., Nieuwenhuis, M. G., Posthuma, G., Thijssen, J. H., Vroom, T. M., Ahren, B., and Lips, C. J. (1999) Extensive islet amyloid formation is induced by development of Type II diabetes mellitus and contributes to its progression: pathogenesis of diabetes in a mouse model. *Diabetologia 42*, 427–434.
10. Butler, A. E., Janson, J., Bonner-Weir, S., Ritzel, R., Rizza, R. A., and Butler, P. C. (2003) Beta-cell deficit and increased beta-cell apoptosis in humans with type 2 diabetes. *Diabetes 52*, 102–110.
11. Butler, A. E., Jang, J., Gurlo, T., Carty, M. D., Soeller, W. C., and Butler, P. C. (2004) Diabetes due to a progressive defect in beta-cell mass in rats transgenic for human islet amyloid polypeptide (HIP Rat): a new model for type 2 diabetes. *Diabetes 53*, 1509–1516.
12. Lorenzo, A., Razzaboni, B., Weir, G. C., and Yankner, B. A. (1994) Pancreatic islet cell toxicity of amylin associated with type-2 diabetes mellitus. *Nature 368*, 756–760.
13. Kayed, R., Head, E., Thompson, J. L., McIntire, T. M., Milton, S. C., Cotman, C. W., and Glabe, C. G. (2003) Common structure of soluble amyloid oligomers implies common mechanism of pathogenesis. *Science 300*, 486–489.
14. Haataja, L., Gurlo, T., Huang, C. J., and Butler, P. C. (2008) Islet amyloid in type 2 diabetes, and the toxic oligomer hypothesis. *Endocr. Rev. 29*, 303–316.
15. Meier, J. J., Kayed, R., Lin, C. Y., Gurlo, T., Haataja, L., Jayasinghe, S., Langen, R., Glabe, C. G., and Butler, P. C. (2006) Inhibition of human IAPP fibril formation does not prevent beta-cell death: evidence for distinct actions of oligomers and fibrils of human IAPP. *Am. J. Physiol.: Endocrinol. Metab. 291*, E1317−1324.
16. Hardy, J., and Selkoe, D. J. (2002) The amyloid hypothesis of Alzheimer′s disease: progress and problems on the road to therapeutics. *Science 297*, 353–356.
17. Jayasinghe, S. A., and Langen, R. (2007) Membrane interaction of islet amyloid polypeptide. *Biochim. Biophys. Acta 1768*, 2002–2009.
18. Nishi, M., Sanke, T., Nagamatsu, S., Bell, G. I., and Steiner, D. F. (1990) Islet amyloid polypeptide. A new beta cell secretory product related to islet amyloid deposits. *J. Biol. Chem. 265*, 4173–4176.
19. Kudva, Y. C., Mueske, C., Butler, P. C., and Eberhardt, N. L. (1998) A novel assay in vitro of human islet amyloid polypeptide amyloidogenesis and effects of insulin secretory vesicle peptides on amyloid formation. *Biochem. J. 331 (Pt 3)*, 809–813.
20. Westermark, P., Li, Z. C., Westermark, G. T., Leckstrom, A., and Steiner, D. F. (1996) Effects of beta cell granule components on human islet amyloid polypeptide fibril formation. *FEBS Lett. 379*, 203–206.
21. Janciauskiene, S., Eriksson, S., Carlemalm, E., and Ahren, B. (1997) B cell granule peptides affect human islet amyloid polypeptide (IAPP) fibril formation in vitro. *Biochem. Biophys. Res. Commun. 236*, 580–585.
22. Jaikaran, E. T., Nilsson, M. R., and Clark, A. (2004) Pancreatic beta-cell granule peptides form heteromolecular complexes which inhibit islet amyloid polypeptide fibril formation. *Biochem. J. 377*, 709–716.
23. Gilead, S., Wolfenson, H., and Gazit, E. (2006) Molecular mapping of the recognition interface between the islet amyloid polypeptide and insulin. *Angew. Chem., Int. Ed. 45*, 6476–6480.
24. Larson, J. L., and Miranker, A. D. (2004) The mechanism of insulin action on islet amyloid polypeptide fiber formation. *J. Mol. Biol. 335*, 221–231.
25. Knight, J. D., Williamson, J. A., and Miranker, A. D. (2008) Interaction of membrane-bound islet amyloid polypeptide with soluble and crystalline insulin. *Protein Sci. 17*, 1850–1856.
26. Padrick, S. B., and Miranker, A. D. (2001) Islet amyloid polypeptide: identification of long-range contacts and local order on the fibrillogenesis pathway. *J. Mol. Biol. 308*, 783–794.
27. Engel, M. F., Yigittop, H., Elgersma, R. C., Rijkers, D. T., Liskamp, R. M., de Kruijff, B., Hoppener, J. W., and Antoinette Killian, J. (2006) Islet amyloid polypeptide inserts into phospholipid monolayers as monomer. *J. Mol. Biol. 356*, 783–789.
28. Lopes, D. H., Meister, A., Gohlke, A., Hauser, A., Blume, A., and Winter, R. (2007) Mechanism of islet amyloid polypeptide fibrillation at lipid interfaces studied by infrared reflection absorption spectroscopy. *Biophys. J. 93*, 3132–3141.
29. Knight, J. D., Hebda, J. A., and Miranker, A. D. (2006) Conserved and cooperative assembly of membrane-bound α-helical states of islet amyloid polypeptide. *Biochemistry 45*, 9496–9508.
30. Williamson, J. A., and Miranker, A. D. (2007) Direct detection of transient α-helical states in islet amyloid polypeptide. *Protein Sci. 16*, 110–117.
31. Tollinger, M., Skrynnikov, N. R., Mulder, F. A., Forman-Kay, J. D., and Kay, L. E. (2001) Slow dynamics in folded and unfolded states of an SH3 domain. *J. Am. Chem. Soc. 123*, 11341–11352.
32. Guntert, P. (2004) Automated NMR structure calculation with CYANA. *Methods Mol. Biol. (Totowa, NJ, U.S.) 278*, 353–378.
33. Sugita, Y., and Okamoto, Y. (1999) Replica-exchange molecular dynamics method for protein folding. *Chem. Phys. Lett. 314*, 141–151.
34. Mu, Y., Nordenskiold, L., and Tam, J. P. (2006) Folding, Misfolding, and Amyloid Protofibril Formation of WW Domain FBP28. *Biophys. J. 90*, 3983–3992.
35. Van der Spoel, D., Lindahl, E., Hess, B., Groenhof, G., Mark, A. E., and Berendsen, H. J. C. (2005) GROMACS: Fast, flexible, and free. *J. Comput. Chem. 26*, 1701–1718.
36. Kaminski, G. A., Friesner, R. A., Tirado-Rives, J., and Jorgensen, W. L. (2001) Evaluation and Reparametrization of the OPLS-AA Force Field for Proteins via Comparison with Accurate Quantum Chemical Calculations on Peptides. *J. Phys. Chem. B 105*, 6474–6487.
37. Hess, B., Bekker, H., Berendsen, H. J. C., and Fraaije, J. (1997) LINCS: A linear constraint solver for molecular simulations. *J. Comput. Chem. 18*, 1463–1472.
38. Darden, T., York, D., and Pedersen, L. (1993) Particle mesh Ewald: An N•log(N) method for Ewald sums in large systems. *J. Chem. Phys. 98*, 10089–10092.
39. Myszka, D. G. (1999) Improving biosensor analysis. *J. Mol. Recognit. 12*, 279–284.
40. Wishart, D. S., Sykes, B. D., and Richards, F. M. (1991) Relationship between nuclear magnetic resonance chemical shift and protein secondary structure. *J. Mol. Biol. 222*, 311–333.
41. Spera, S., and Bax, A. (1991) Empirical correlation between protein backbone conformation and Cα and Cβ 13C nuclear magnetic resonance chemical shifts. *J. Am. Chem. Soc. 113*, 5490–5492.
42. Daura, X., Gademann, K., Jaun, B., Seebach, D., van Gunsteren, W. F., and Mark, A. E. (1999) Peptide folding: When simulation meets experiment. *Angew. Chem., Int. Ed. 38*, 236–240.
43. Marek, P., Abedini, A., Song, B., Kanungo, M., Johnson, M. E., Gupta, R., Zaman, W., Wong, S. S., and Raleigh, D. P. (2007) Aromatic interactions are not required for amyloid fibril formation by islet amyloid polypeptide but do influence the rate of fibril formation and fibril morphology. *Biochemistry 46*, 3255–3261.
44. Jaikaran, E. T., Higham, C. E., Serpell, L. C., Zurdo, J., Gross, M., Clark, A., and Fraser, P. E. (2001) Identification of a novel human islet amyloid polypeptide beta-sheet domain and factors influencing fibrillogenesis. *J. Mol. Biol. 308*, 515–525.
45. Mazor, Y., Gilead, S., Benhar, I., and Gazit, E. (2002) Identification and characterization of a novel molecular-recognition and self-assembly domain within the islet amyloid polypeptide. *J. Mol. Biol. 322*, 1013–1024.
46. Scrocchi, L. A., Ha, K., Chen, Y., Wu, L., Wang, F., and Fraser, P. E. (2003) Identification of minimal peptide sequences in the (8−20) domain of human islet amyloid polypeptide involved in fibrillogenesis. *J. Struct. Biol. 141*, 218–227.
47. Goldsbury, C., Goldie, K., Pellaud, J., Seelig, J., Frey, P., Muller, S. A., Kistler, J., Cooper, G. J., and Aebi, U. (2000) Amyloid fibril formation from full-length and fragments of amylin. *J. Struct. Biol. 130*, 352–362.
48. Moriarty, D. F., and Raleigh, D. P. (1999) Effects of sequential proline substitutions on amyloid formation by human amylin 20−29. *Biochemistry 38*, 1811–1818.
49. Mascioni, A., Porcelli, F., Ilangovan, U., Ramamoorthy, A., and Venglia, G. (2003) Conformational preferences of the amylin nucleation site in SDS micelles: an NMR study. *Biopolymers 69*, 29–41.

50. Brender, J. R., Durr, U. H., Heyl, D., Budarapu, M. B., and Ramamoorthy, A. (2007) Membrane fragmentation by an amyloidogenic fragment of human Islet Amyloid Polypeptide detected by solid-state NMR spectroscopy of membrane nanotubes. *Biochim. Biophys. Acta 1768*, 2026–2029.
51. Brender, J. R., Lee, E. L., Cavitt, M. A., Gafni, A., Steel, D. G., and Ramamoorthy, A. (2008) Amyloid fiber formation and membrane disruption are separate processes localized in two distinct regions of IAPP, the type-2-diabetes-related peptide. *J. Am. Chem. Soc. 130*, 6424–6429.
52. Knight, J. D., and Miranker, A. D. (2004) Phospholipid catalysis of diabetic amyloid assembly. *J. Mol. Biol. 341*, 1175–1187.
53. Nanga, R. P., Brender, J. R., Xu, J., Veglia, G., and Ramamoorthy, A. (2008) Structures of Rat and Human Islet Amyloid Polypeptide IAPP 1−19 in Micelles by NMR Spectroscopy. *Biochemistry 47*, 12689–12697.
54. LeVine, H., III (2002) 4,4(′)-Dianilino-1,1(′)-binaphthyl-5,5(′)-disulfonate: report on non-beta-sheet conformers of Alzheimer's peptide beta(1−40). *Arch. Biochem. Biophys. 404*, 106–115.
55. Kirkitadze, M. D., Condron, M. M., and Teplow, D. B. (2001) Identification and characterization of key kinetic intermediates in amyloid beta-protein fibrillogenesis. *J. Mol. Biol. 312*, 1103–1119.
56. Thompson, R. G., Gottlieb, A., Organ, K., Koda, J., Kisicki, J., and Kolterman, O. G. (1997) Pramlintide: a human amylin analogue reduced postprandial plasma glucose, insulin, and C-peptide concentrations in patients with type 2 diabetes. *Diabetic Med. 14*, 547–555.
57. Hekman, C. M., DeMond, W. S., Kelley, P. J., Mauch, S. F., and Williams, J. D. (1999) Isolation and identification of cyclic imide and deamidation products in heat stressed pramlintide injection drug product. *J. Pharm. Biomed. Anal. 20*, 763–772.
58. Wishart, D. S., Bigam, C. G., Holm, A., Hodges, R. S., and Sykes, B. D. (1995) 1H, 13C and 15N random coil NMR chemical shifts of the common amino acids. I. Investigations of nearest-neighbor effects. *J. Biomol. NMR 5*, 67–81.

BI802097B